Flexoelectricity as a universal mechanism for energy harvesting from crumpling of thin sheets

Binglei Wang, Shengyou Yang, and Pradeep Sharma

Phys. Rev. B **100**, 035438 — Published 29 July 2019

DOI: 10.1103/PhysRevB.100.035438

Flexoelectricity as a universal mechanism for energy harvesting from crumpling of thin sheets

Binglei Wang[1,2†], Shengyou Yang[2†] and Pradeep Sharma[2,3‡]
[1] *School of Civil Engineering, Shandong University, Jinan, 250061, China*
[2] *Department of Mechanical Engineering, University of Houston, Houston, TX 77204, USA*
[3] *Department of Physics, University of Houston, Houston, TX 77204, USA*
[‡] *Corresponding Author: psharma@uh.edu*
[†] *Wang and Yang contributed equally to this work*

Can the mere crumpling of a "paper" produce electricity? An inhomogeneous strain can induce electrical response in *all* dielectrics and not just piezoelectric materials. This phenomenon of *flexoelectricity* is rather modest unless unusually large strain gradients are present. In this work, we analyze the crumpling of thin elastic sheets and establish scaling laws for their electromechanical behavior to prove that an extremely strong flexoelectric response is achieved at sub-micron length-scales. Connecting with recent experiments on crumpling of a polymer paper, we argue that crumpling is a viable energy harvesting route with applications in wearable electronics and related contexts.

I. INTRODUCTION

Crumpling of flat sheets is ubiquitous in our daily lives. The inevitable deposition of a used (and crumpled) paper before its relegation to the recycling bin provides but just one example. This phenomenon has attracted much attention and heretofore studied purely as a mechanical and geometrical problem [1–7]. Indeed, the mechanics of crumpling is quite rich, and the intricate coupling between deformation energy stored in stretching, bending and subtle differential geometric aspects pertaining to 2D structures has bearing on problems as diverse as the shape of flowers to speed of earthquakes [8].

FIG. 1. Schematic of the electricity generated due to the crumpling of a thin dielectric sheet. Large strain gradients at the sharp tips in the crumpling sheet may polarize the material due to the phenomenon of flexoelectricity.

Is crumpling truly a purely mechanical problem? For materials that are not piezoelectric, the answer would appear to be in the affirmative. However, this ignores a rather under-appreciated phenomenon that has attracted much recent attention. *Flexoelectricity* is a universal electro-mechanical coupling between strain-*gradients* and polarization [9–17]. It's universal nature is to be emphasized since it exists, in principle, in all (insulating) materials and has paved the way for fascinating applications such as piezoelectric materials without using piezoelectric materials [17–20], nanoscale energy harvesting [21–24], ferroelectric domain engineering [25–27], sensors and actuators [28–30], defects [31], and biomedicine [32–34] among others. In a conventional piezoelectric material, electricity (or electric polarization, $\boldsymbol{p}$) can be generated through the piezoelectric effect:

$$p_i \sim d_{ijk}\epsilon_{jk}, \tag{1}$$

where d_{ijk} denote the components of the third-order piezoelectric tensor and ϵ_{jk} are the strain tensor components. Here we have used index notation and Cartesian basis to make explicit the order of the material property tensors as well make comments about symmetry. Piezoelectricity only exists in a few special materials (that have a non-centrosymmetric crystalline structure). In contrast, if flexoelectricity is accounted for, the polarization takes the form:

$$p_i \sim d_{ijk}\epsilon_{jk} + f_{ijkl}\frac{\partial \epsilon_{jk}}{\partial x_l}, \tag{2}$$

where f_{ijkl} are the components of the fourth-order flexoelectric tensor.

A most notable characteristic of flexoelectricity is the size-dependency inherent in its response. As numerous works have shown, and as may be evident from its reliance on gradients of strain (which imparts a nonlocal character to the phenomenon), the flexoelectric response increases dramatically when the feature size of

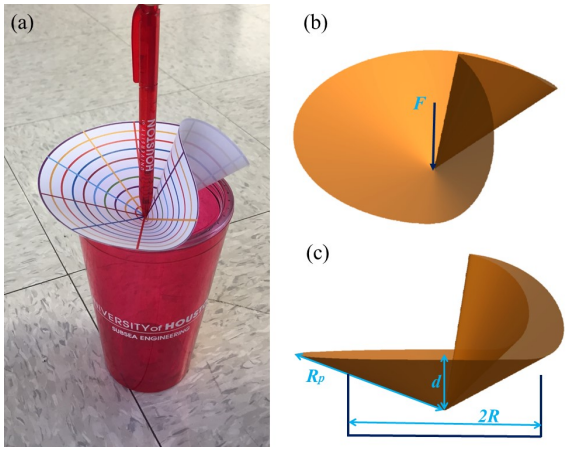

FIG. 2. A crumpled thin sheet: (a) The crumpled shape of a circular paper with radius R_p resting on a cup with radius R. The crumpled shape is generaed by applying a concentrated load F at the central point of the paper. Parts (b) top view and (c) front view, show the geometry underpinning the crumpling state.

the dielectric structure shrinks to submicron or nanoscale [17, 21, 23, 35]. The simple bending of a thin "paper" or paper-like structure ought to activate a flexoelectric response–a fact amply demonstrated in the case of atomically thin 2D materials like graphene and others [20, 34, 36]. However, the electrical energy gain would be rather modest since the flexoelectric coefficients of most materials are rather small—unless very high curvatures are induced. The latter is most facile when the underlying geometric feature size (–thickness in this instance) is at the nanoscale. Crumpling, provides a rather interesting alternative to generate large localized strain gradients (or in this context, changes in curvature). Recently, Kodali et al. [37] proposed to generate electric power from the crumpling of micron-thick polymer *piezoelectric* foils for wearable electronics and experimentally observed the development of a voltage (≈ 0.1V). Recognizing the potential of crumpling to induce a significant flexoelectric response, we argue that crumpling could provide a facile route to generate electric power in thin paper-like structures of *all* materials (and not just piezoelectric). Fig. 1 shows the basic concept underlying the present work of power production from crumpling of a thin dielectric sheet.

Before outlining some of the novel aspects of the present work, it is imperative to briefly recapitulate the current understanding of the crumpling problem from a purely mechanical and geometric viewpoint. The simplest example of a crumpled sheet is a developable cone (d-cone), which is a deformed circular sheet under a central point force perpendicular to the original flat sheet constrained by a cylinder. This is shown in Fig. 2(a) and as evident, may be created on a regular office printer paper. The point-like singularities (Fig. 2(b)) that appear on a crumpling elastic sheet, as a result of stress focusing, have been recently the subject of several investigations [1, 38, 39]. To analytically model the developable cone, Cerda and Mahadevan [3, 6] presented an analytical solution for the universal shape of a d-cone with singularities and also gave a scaling relation for the core size [5]. Somewhat complementarily, ChaÏeb and Melo [4] carried out an experiment to investigate d-cones topology, and calculated the angle ($\approx 120°$) over which the developable cone is not in contact with the edge of the cylinder. This angle, however, is a little different from what Cerda and Mahadevan estimated ($\approx 140°$) [3], which is shown in Fig. 2(c). Recently, Müller and Olbermann [40] improved the scaling law of the elastic energy of d-cones by following the work of Brandman [41].

In a departure from the works quoted in the preceding paragraphs, Kodali et al. [37] examined crumples in composite piezoelectric thin sheets. Specifically, they embedded sheets of a polymer piezoelectric (PVDF) in clothing in which power is generated by crumpling of clothes due to human body movements. They showed that a nontrivial voltage is generated from a single d-cone crumple and presented a scaling law relating the geometry of the crumpling d-cone and the generated open circuit voltage and short circuit current.

Our work, motivated by the generated voltage in the developable cone [37], is predicated on the observation that at the tip of the d-cone, not only the strain is considerable, but so is the strain gradient (i.e., curvature). Taking cognizance of Eq. (2), polarization may be induced by *both* piezoelectricity (if the material is piezoelectric) and flexoelectricity (in all dielectrics). So the following questions may be asked both from the viewpoint of fundamental physics as well as potential applications: (1) Given that flexoelectricity is universal, what is the *correct* interpretation of the experiments of Kodali et. al. [37] on electricity generated by PVDF paper? (2) What is the mechanics and physics of crumpling if flexoelectricity is accounted for? (3) What are the pertinent electromechanical scaling laws? (4) Is the energy harvested viable or at least comparable to what might be obtained from analogous crumpling of piezoelectric materials? In this work, we seek to answer the questions posed in the preceding paragraph. In particular, in this work, we focus on the possibility of generating electric power from the universal flexoelectric response of a crumpling dielectric sheet.

II. THEORETICAL FORMULATION FOR THE CRUMPLING OF A THIN ELASTIC SHEET WITH PIEZOELECTRICITY AND FLEXOELECTRICITY

We now briefly sketch out the central aspects of the theoretical formulation for crumpling of a thin elastic sheet incorporating both flexoelectricity and piezoelectricity. While the latter is not the focus of this work, in order to connect with recent experiments, we address

piezoelectricity also. Most of the details related to the theory are recorded in the Appendix. The deformation of a crumpling sheet is shown in Fig. 2(a). A vertical force F is applied to push the central point of the flat circular sheet (with radius of R_p), which is centrally placed on the supporting hoop (with inner radius R). The thin sheet bends up to the depth d when F is very small. However, crumpling ensues once F is increased sufficiently. Consider the domain occupied by a continuum body in the space is denoted by $\mathcal{B}$ with the boundary $\partial\mathcal{B}$. In general, the deformation of the body $\mathcal{B}$ can be expressed by a mapping $\boldsymbol{y} : \mathcal{B} \to \mathbb{R}^3$. A representative material point of the body is $\boldsymbol{x} \in \mathcal{B}$. In contrast, the spatial point is $\boldsymbol{y} = \boldsymbol{y}(\boldsymbol{x}) = \boldsymbol{x} + \boldsymbol{u}$, where $\boldsymbol{u}$ is the displacement vector. The displacement and electric potential (ξ) boundary conditions may be specified on the respective surface domains as detailed in the Appendix.

The total potential energy associated with the deformed electrostatic system is given by

$$\begin{aligned}\mathcal{F}[\boldsymbol{u},\boldsymbol{p},\xi] = \int_{\mathcal{B}} \left\{ W - \frac{1}{2}\epsilon_0 |\nabla\xi|^2 + \boldsymbol{p}\cdot\nabla\xi \right\} dv \\ - \int_{\partial\mathcal{B}_d} \xi Q ds - \int_{\partial\mathcal{B}_t} \boldsymbol{t}\cdot\boldsymbol{u} ds,\end{aligned} \tag{3}$$

where $W(\nabla\boldsymbol{u}, \nabla\nabla\boldsymbol{u}, \boldsymbol{p})$ is the internal energy function, ϵ_0 is the vacuum permittivity, $\boldsymbol{p}$ is the polarization, Q is the surface charge density, and $\boldsymbol{t}$ is the applied deadload.

The Euler-Lagrange equations and the natural boundary conditions can be determined by minimizing the total potential energy: $\min_{\forall(\boldsymbol{u},\boldsymbol{p},\xi)\in\mathbb{S}} \mathcal{F}[\boldsymbol{u},\boldsymbol{p},\xi]$, where the minimization is carried out over a suitable admissible space $\mathbb{S}$. We omit further details here and refer the reader to the Appendix. After using the relevant kinematic assumptions for thin bodies, suitable constitutive choices and other aspects elaborated in the Appendix, we obtain the following key result for a thin elastic dielectric sheet. The total energy (3) specialized to a thin sheet with thickness h becomes

$$\mathcal{F}[\boldsymbol{u}] = \frac{1}{2}\int_{\mathcal{S}} W_s ds - Fd, \tag{4}$$

where the two-dimensional energy function W_s is

$$W_s = \boldsymbol{E}_s \cdot \mathbb{C}_s \boldsymbol{E}_s + (K_s + K_s^*)[\mathrm{tr}(\boldsymbol{\kappa})]^2. \tag{5}$$

Here the coefficients K_s and K_s^* are

$$K_s = C_b + hg - ha^* f_s^2, \quad K_s^* = -ha^* f_s^2(\eta^2 + 2\eta) \tag{6}$$

with the ratio $\eta = d_s \mathrm{tr}(\boldsymbol{E}_s)/[f_s \mathrm{tr}(\boldsymbol{\kappa})]$.

Here, $\boldsymbol{E}_s$ is the in-plane strain tensor and $\boldsymbol{\kappa}$ is the curvature tensor. The material properties are parametrized by $\mathbb{C}_s$ which is the in-plane stiffness tensor, and by C_b which is the bending stiffness. The property g parametrizes the elastic cost of strain gradients and in the context of thin sheets (as opposed to three-dimensional bodies) merely renormalizes the bending modulus. The other terms (d_s, f_s, a^*) are related to the piezoelectricity, flexoelectricity and dielectric permittivity of the sheet and are defined in detail in the SI. Typically, in the case of non-piezoelectricity, $d_s = 0$, the ratio η and the coefficient K_s^* in Eq. (6) are zero. As shown in Fig. 2, the crumpling sheet deforms into a non-axisymmetric conical surface that is in partial contact with the supporting hoop. To model the developable cone, the middle surface $\mathcal{S}$ of the dielectric sheet is divided into two parts: $\mathcal{S}^c = \{\boldsymbol{x} \in \mathcal{S} : 0 \leqslant \rho \leqslant R_c\}$, $\mathcal{S}^d = \mathcal{S} \setminus \mathcal{S}^c$. The *core* part $\mathcal{S}^c$ is the region near the tip of the developable cone and R_c can be interpreted as the core size [5, 6]. The core part of a crumpling sheet is analogous to the core of a dislocation [3, 42]. In addition, the outer region of the developable cone is $\mathcal{S}^d$. We remark that the variation of the local curvature along the developable cone (d-cone) separates the d-cone into two parts [3, 4]: in terms of the azimuthal angle (θ) the concave part ($-\theta_1 \leqslant \theta \leqslant \theta_1$) and the convex part ($\theta_1 \leqslant \theta \leqslant 2\pi - \theta_1$). In the convex part, the surface fully contacts the hoop and forms a near-perfect circular cone except near its tip or core; while in the concave part the d-cone loses contact with the supporting hoop. For the purely mechanical problem, we note that Cerda and Mahadevan [3] predicted the angle (θ_1) to be: $\theta_1 \approx 70^\circ$ while $\theta_1 \approx 60^\circ$ was estimated by Chaieb et al. [4]. Finally, the conical shape of a crumpling sheet can be completely parametrized by two non-dimensional numbers: ($\alpha_1 = d/R, \alpha_2 = R_c/R$) which are the proxies for (d, R_c): the tip displacement and the core radius (see the Appendix). Thus the dimensionless numbers (α_1, α_2) are the two unknown quantities which are determined by the variational principle described earlier. Due to the nonlinear nature of the problem, the final results are obtained numerically.

III. RESULTS AND DISCUSSIONS

Before interrogating our model for insights into crumpling induced energy harvesting, we believe it is worthwhile to validate its prediction against established literature for the purely mechanical case. Using identical geometrical and material parameters as those reported in [5], we compared the results of the prediction of our model (see the Appendix) for the purely mechanical case (i.e. with piezoelectricity and flexoelectricity suppressed) and found excellent agreement for small deformation between our model predictions and the experimental data in [5]. For relatively large deformation, the agreement is not perfect but accounting for that is not the focus of this work. Our central goal is to achieve sufficient accuracy (and correct qualitative behavior) to account for piezoelectric and flexoelectric response of crumpling sheets, which we now discuss next.

In their experiments, Kodali et al. [37] measured the open circuit voltage and the short circuit current of a crumpling circular composite sheet. The composite sheet was made of a $52\mu m$ thick poly vinyldenefluo-

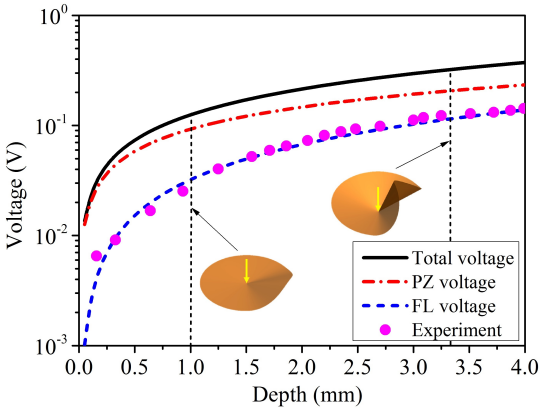

FIG. 3. Comparison of the generated voltage of a crumpling sheet predicted by our model with the experimental data of Kodali et al. [37]. The generated voltage *vs* the tip depth d of the crumpling circular sheet is plotted. In our model, we consider both the contributions of piezoelectricity and flexoelectricity while the experiments can only calibrate the total voltage on the upper and bottom surfaces of a crumpling sheet.

ride (PVDF)—a known piezoelectric polymer—with electrodes on both sides and bonded to a soft cloth-plaster. The circular sheet was placed on a supporting hoop and then a concentrated vertical force was applied at the sheet center to form the crumpled configuration. For different radii of the supporting hoop $R = (12.5, 20, 25)mm$, roughly $0.1\ V$ was measured by pushing the center of the circular sheet (with radius $50mm$) into a supporting hoop up to the maximum depth ($\approx 4mm$). Kodali et al. attribute the observed induced voltage to the piezoelectric effect exhibited by PVDF. Our hypothesis is that, since flexoelectricity cannot be "turned-off", the observed potential difference is due to *both* phenomena. What are their relative contributions? We report some surprising and interesting insights below.

In our theoretical model, the flexoelectric constant is chosen as $f_s = -179Nm/C$ [17, 21]. The geometrical and material parameters of a circular composite sheet in the crumpling experiment [37] are: $R_p = 50mm$, $h = 52\mu m$, $E = 5GPa$, $d_{31} = 5pC/N$, and $\epsilon = 88.5 \times 10^{-12}F/m$. Using our model, we partition the total voltage obtained into that due to flexoelectricity (FL voltage) and piezoelectricity (PZ voltage). As elaborated in the SI, the nonlocal elastic constant g has a negligible effect on the comparison with experiments since sheet thickness in the experiments is quite large compared to the characteristic nonlocal length scale.

Fig. 3 shows how the induced voltage varies with the increase of the tip deflection d where we also compare our model predictions with the experimental data from Ref. [37]. The radius of the supporting hoop is taken to be $R = 12.5mm$. The developed potential difference increases to $0.14V$ as the tip deflection increases to $4mm$. Thus the electric field in the $52\mu m$ thickness film can be as high as $3 \times 10^3 V/m$, which is considerable when placed in the context of soft dielectrics. The key insight is that our flexoelectricity based model is able to predict the generated voltage including both piezoelectricity and flexoelectricity. More importantly, both voltages are comparable to each other and are of the same order as the experimental data reported by Kodali et al. [37]. Notably, our model shows that the flexoelectricity leads to a non-trivial contribution to the generated voltage of a crumpled sheet at microscale and cannot be ignored. In addition due to the size-dependency inherent in the phenomenon of flexoelectricity (which is *absent* in piezoelectricity), it becomes dominant when the film thickness decreases from microscale to nanoscale. This is articulated in Fig. 4 in terms of the variation of the electromechanical coupling with respect to film thickness. Explicitly, the piezoelectricity in our model originates from the in-plane strain $\boldsymbol{E}_s$ of the core part while the flexoelectricity results from the curvature of the crumpled film, see Eq. (6) or Eq. (A20). Physically, this may be rationalized in the following way. For a piezoelectric material (like PVDF) attached to a very thin soft cloth, it is unlikely that bending will contribute significantly to a piezoelectric response (since compression and tension below and above the neutral axis of the material will produce significant cancellation). This is however not the case for flexoelectricity. We remark that in the case of inextensible films, piezoelectricity "turns off" but flexoelectricity does contribute, i.e., crumpling induced electricity is essentially mediated by bending in the case of inextensible materials. Needless to say that as evident from Fig. 3, crumpling induced mechanical energy can be converted to the electrical energy.

A major consequence of the establishment of the scaling relation for flexoelectricity in crumpling is that we are now in a position to go beyond known experiments and examine the size-dependency of the electromechanical coupling. As noted earlier, piezoelectricity does not produce any size-effects while the flexoelectric effect is size-dependent c.f.[17]. We define and focus on the emergent electromechanical coupling that is defined as the ratio of the induced charge Q on the sheet surface in response to the applied force F, namely $d^{\text{eff}} = Q/F$. Such a definition can be considered as the amount of electric charge (including the contribution of both piezoelectricity and flexoelectricity) produced by per unit of applied force. As a point of comparision, for a common crystalline piezoelectric material like barium titanate, this coefficient is around $d^{\text{BaTiO}_3} = 78pC/N$. In the crumpling of a thin sheet with thickness $h = 52\mu m$ used in Fig. 3, for instance, the effective effect at a tip deflection $d = 4mm$ is found to be $d^{\text{eff}} = 250pC/N$ from the experimental data [37]. As demonstrated in Fig. 4, as the thickness of the sheet is reduced to around $100nm$, the electromechanical coupling reaches values close to $65000pC/N$. In the plot, we chose the same basic parameters in Fig. 3 as the starting point, and the geometry of the sheet was scaled

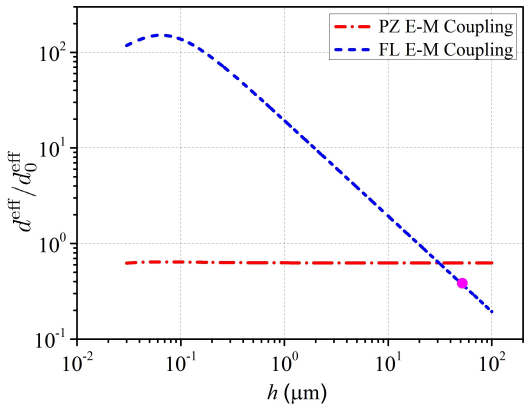

FIG. 4. Flexoelectric and piezoelectric effects *vs* the sheet thickness h. The effective effect (electromechanical coupling) is defined as $d^{\text{eff}} = Q/F$, and is normalized by $d_0^{\text{eff}} = 652pC/N$ that is calculated by the geometrical and material parameters in Fig. 3 at tip depth $d = 4mm$. The experimental data (solid circle, $d^{\text{eff}}/d_0^{\text{eff}} = 0.38$) of the effective effect of a thin sheet with thickness $h = 52\mu m$ is also plotted for comparison between different thicknesses. The reported piezoelectric coefficient of barium titanate is around $d^{\text{BaTiO}_3} = 78pC/N$.

as: $(R_p : R : h : d) = \gamma(50mm : 12.5mm : 52\mu m : 4mm)$, where γ is a nondimensional scale factor and $\gamma = 1$ corresponds to the size of thin sheet in Fig. 3. By changing the scale factor γ, we can make the sheet thickness h ranging from $10nm$ to $100\mu m$. We chose $d_0^{\text{eff}} = 650pC/N$ to normalize the effective piezoelectric and flexoelectric effects in Fig. 4 at different thicknesses. The piezoelectric effect is insensitive to the scale of thin sheets, however, the flexoelectric effect remarkably increases (two orders) as the thickness decreases from several microns to a few nanometers.

APPENDICES

Appendix A: The detailed theoretical formulation

1. Energy minimization of an electrostatic system

The domain occupied by a continuum body in the space is denoted by $\mathcal{B}$ with the boundary $\partial\mathcal{B}$. In general, the deformation of the body $\mathcal{B}$ can be expressed by a mapping $\boldsymbol{y} : \mathcal{B} \to \mathbb{R}^3$. A representative material point of the body is $\boldsymbol{x} \in \mathcal{B}$. In contrast, the spatial point is $\boldsymbol{y} = \boldsymbol{y}(\boldsymbol{x}) = \boldsymbol{x} + \boldsymbol{u}$, where $\boldsymbol{u}$ is the displacement vector.

The boundary conditions of the displacement $\boldsymbol{u}$ and the displacement gradient $\nabla\boldsymbol{u}$ are

$$\boldsymbol{u} = \boldsymbol{u}_0, \quad \boldsymbol{n}\cdot(\nabla\boldsymbol{u})\boldsymbol{n} = \boldsymbol{n}\cdot(\nabla\boldsymbol{u}_0)\boldsymbol{n} \quad \text{on } \partial\mathcal{B}_u, \tag{A1}$$

where $\boldsymbol{n}$ is the outward unit normal to the surface $\partial\mathcal{B}_u$, $\boldsymbol{u}_0$ is the prescribed displacement vector, and the normal derivative of the displacement vector is also prescribed. For simplicity, we assume that the displacement boundary and normal derivative boundary conditions are at $\partial\mathcal{B}_u$. In contrast, the traction boundary and higher-order traction boundary conditions are at $\partial\mathcal{B}_t = \partial\mathcal{B} \setminus \partial\mathcal{B}_u$.

The electric boundary condition of the electric potential ξ is

$$\xi = \xi_0 \quad \text{on } \partial\mathcal{B}_\xi, \tag{A2}$$

where ξ_0 is the prescribed potential. The surface charge boundary condition is at $\partial\mathcal{B}_d = \partial\mathcal{B} \setminus \partial\mathcal{B}_\xi$.

The total potential energy associated with the deformed electrostatic system is given by

$$\begin{aligned}\mathcal{F}[\boldsymbol{u},\boldsymbol{p},\xi] = &\int_{\mathcal{B}} \left\{ W - \frac{1}{2}\epsilon_0|\nabla\xi|^2 + \boldsymbol{p}\cdot\nabla\xi \right\} dv \\ &- \int_{\partial\mathcal{B}_d} \xi Q ds - \int_{\partial\mathcal{B}_t} \boldsymbol{t}\cdot\boldsymbol{u} ds,\end{aligned} \tag{A3}$$

where $W(\nabla\boldsymbol{u}, \nabla\nabla\boldsymbol{u}, \boldsymbol{p})$ is the internal energy function, ϵ_0 is the vacuum permittivity, $\boldsymbol{p}$ is the polarization, Q is the surface charge density, and $\boldsymbol{t}$ is the applied dead load.

The Euler-Lagrange equations and the natural boundary conditions can be determined by minimizing the total potential energy:

$$\min_{\forall(\boldsymbol{u},\boldsymbol{p},\xi)\in\mathbb{S}} \mathcal{F}[\boldsymbol{u},\boldsymbol{p},\xi], \tag{A4}$$

where the admissible space $\mathbb{S}$ for $(\boldsymbol{u},\boldsymbol{p},\xi)$ is given by

$$\mathbb{S} = \left\{ Eq.(\text{A1}), Eq.(\text{A2}), \int_{\mathcal{B}} |\nabla\boldsymbol{u}|^2, |\nabla\nabla\boldsymbol{u}|^2, |\boldsymbol{p}|^2, |\nabla\xi|^2 < +\infty \right\}.$$

The minimization problem leads to the zero first variation $\delta\mathcal{F} = 0$, namely

$$\delta\mathcal{F}[\boldsymbol{u},\boldsymbol{p},\xi] := \frac{d}{d\tau}\mathcal{F}[\boldsymbol{u}+\tau\boldsymbol{u}_1, \boldsymbol{p}+\tau\boldsymbol{p}_1, \xi+\tau\xi_1]|_{\tau=0} = 0, \tag{A5}$$

where $\tau \in \mathbb{R}$, and $\boldsymbol{u}_1$, $\boldsymbol{p}_1$, ξ_1 are the admissible variations of $\boldsymbol{u}$, $\boldsymbol{p}$, ξ, respectively. The variations $(\boldsymbol{u}_1, \boldsymbol{p}_1, \xi_1)$ have to satisfy the following conditions

$$\boldsymbol{u}_1 = \boldsymbol{0}, \quad \boldsymbol{n}\cdot(\nabla\boldsymbol{u}_1)\boldsymbol{n} = 0 \quad \text{on } \partial\mathcal{B}_u, \tag{A6a}$$

$$\xi_1 = 0 \quad \text{on } \partial\mathcal{B}_\xi, \tag{A6b}$$

and

$$\left\{ \int_{\mathcal{B}} |\nabla\boldsymbol{u}_1|^2, |\nabla\nabla\boldsymbol{u}_1|^2, |\boldsymbol{p}_1|^2, |\nabla\xi_1|^2 < +\infty \right\}. \tag{A6c}$$

Direct consequences of the zero first variation (A5), together with (A6), are

$$\begin{aligned} \nabla\cdot(\boldsymbol{T}_I-\nabla\cdot\boldsymbol{T}_{II})&=\boldsymbol{0} \quad \text{in } \mathcal{B},\\ W_{\boldsymbol{p}}+\nabla\xi&=\boldsymbol{0} \quad \text{in } \mathcal{B},\\ \nabla\cdot(-\epsilon_0\nabla\xi+\boldsymbol{p})&=0 \quad \text{in } \mathcal{B},\\ (\boldsymbol{T}_I-\nabla\cdot\boldsymbol{T}_{II})\,\boldsymbol{n}-\nabla\cdot([\boldsymbol{T}_{II}]\boldsymbol{n})&=\boldsymbol{t} \quad \text{on } \partial\mathcal{B}_t,\\ [\boldsymbol{T}_{II}]\,\boldsymbol{n}&=\boldsymbol{0} \quad \text{on } \partial\mathcal{B}_t,\\ (-\epsilon_0\nabla\xi+\boldsymbol{p})\cdot\boldsymbol{n}&=Q \quad \text{on } \partial\mathcal{B}_d. \end{aligned} \tag{A7}$$

Here "$\nabla\cdot$" is the divergence operator and $W_{\boldsymbol{p}}=\frac{\partial W}{\partial \boldsymbol{p}}$. $\boldsymbol{T}_I$ is the second-order stress tensor and $\boldsymbol{T}_{II}$ is the third-order stress tensor, namely

$$\boldsymbol{T}_I=\frac{\partial W}{\partial\nabla\boldsymbol{u}},\quad \boldsymbol{T}_{II}=\frac{\partial W}{\partial\nabla\nabla\boldsymbol{u}}. \tag{A8}$$

With a linearized setting, the internal energy function $W(\nabla\boldsymbol{u},\nabla\nabla\boldsymbol{u},\boldsymbol{p})$ can be written as [18, 43]

$$W=W^{elast}+\frac{1}{2}\boldsymbol{p}\cdot\boldsymbol{a}\boldsymbol{p}+\boldsymbol{p}\cdot\boldsymbol{d}\mathbb{I}_2+\boldsymbol{p}\cdot\boldsymbol{f}\mathbb{I}_3+\frac{1}{2}\mathbb{I}_3\cdot\boldsymbol{g}\mathbb{I}_3, \tag{A9}$$

where W^{elast} is the purely elastic energy function, $\mathbb{I}_2=\mathbb{I}_2(\nabla\boldsymbol{u})$ is a second-order tensor related to the strain, and $\mathbb{I}_3=\mathbb{I}_3(\nabla\nabla\boldsymbol{u})$ is a third-order tensor related to the strain gradient. Material parameter $\boldsymbol{a}$ corresponds to the reciprocal dielectric susceptibility, other parameters $\boldsymbol{d}$, $\boldsymbol{f}$, and $\boldsymbol{g}$ are related to the piezoelectric, flexoelectric, and strain gradient effects, respectively.

2. Large deflection of thin films

Consider a flat disc thin film with radius R_p and thickness h. The domain occupied by the flat film is

$$\mathcal{B}=\{(\rho,\theta,z)\in\mathbb{R}^3:0\leqslant\rho\leqslant R_p,0\leqslant|\theta|\leqslant\pi,0\leqslant z\leqslant h\}, \tag{A10}$$

where (ρ,θ,z) are cylindrical coordinates with unit basis $(\hat\rho,\hat\theta,\hat z)$. The material point in cylindrical coordinates is $\boldsymbol{x}=\rho\hat\rho+z\hat z\in\mathcal{B}$. The middle surface of the disc film is

$$\mathcal{S}=\{\boldsymbol{x}\in\mathcal{B}:z=h/2\} \tag{A11}$$

while the upper and lower surfaces are

$$\mathcal{S}_u=\{\boldsymbol{x}\in\mathcal{B}:z=0\}\quad\text{and}\quad\mathcal{S}_l=\{\boldsymbol{x}\in\mathcal{B}:z=h\}. \tag{A12}$$

In addition, the surrounding surface is represented by $\mathcal{S}_s=\partial\mathcal{B}\setminus(\mathcal{S}_u\cup\mathcal{S}_l)$.

Consider the deformation of the middle surface $\mathcal{S}$. A material point $\boldsymbol{x}\in\mathcal{S}$ is deformed to a spatial point $\boldsymbol{y}=\boldsymbol{x}+\boldsymbol{u}\in\mathbb{R}^3$. The displacement vector $\boldsymbol{u}:\mathcal{S}\to\mathbb{R}^3$ is assumed as

$$\boldsymbol{u}=\boldsymbol{u}_s+\boldsymbol{u}_\perp, \tag{A13a}$$

where $\boldsymbol{u}_s$ is the in-plane displacement

$$\boldsymbol{u}_s=u_\rho(\rho,\theta)\hat\rho+u_\theta(\rho,\theta)\hat\theta \tag{A13b}$$

and $\boldsymbol{u}_\perp$ is the out-of-plane deflection

$$\boldsymbol{u}_\perp=\zeta(\rho,\theta)\hat z. \tag{A13c}$$

The in-plane strain tensor of the thin film is defined as [44]

$$\boldsymbol{E}_s=\frac{1}{2}\left(\nabla_s\boldsymbol{u}_s+(\nabla_s\boldsymbol{u}_s)^T+\nabla_s\zeta\otimes\nabla_s\zeta\right), \tag{A14a}$$

where $\nabla_s=\hat\rho\partial_\rho+\hat\theta\rho^{-1}\partial_\theta$ is the two-dimensional (in-plane) gradient operator. By (A13b) and (A13c), the matrix form of $\boldsymbol{E}_s$ in (A14a) is

$$\boldsymbol{E}_s:=\begin{pmatrix}E_{\rho\rho}&E_{\rho\theta}\\E_{\theta\rho}&E_{\theta\theta}\end{pmatrix}, \tag{A14b}$$

where the entries are

$$E_{\rho\rho}=\partial_\rho u_\rho+\frac{1}{2}(\partial_\rho\zeta)^2, \tag{A14c}$$

$$E_{\theta\theta}=\frac{u_\rho}{\rho}+\frac{\partial_\theta u_\theta}{\rho}+\frac{1}{2}\frac{(\partial_\theta\zeta)^2}{\rho^2}, \tag{A14d}$$

$$E_{\rho\theta}=E_{\theta\rho}=\frac{1}{2}\left(\frac{\partial_\theta u_\rho}{\rho}-\frac{u_\theta}{\rho}+\partial_\rho u_\theta+\frac{\partial_\rho\zeta\partial_\theta\zeta}{\rho}\right). \tag{A14e}$$

The (linearized) curvature tensor of the thin film is

$$\boldsymbol{\kappa}=-\nabla_s\nabla_s\zeta(\rho,\theta):=\begin{pmatrix}\kappa_{\rho\rho}&\kappa_{\rho\theta}\\\kappa_{\theta\rho}&\kappa_{\theta\theta}\end{pmatrix}, \tag{A15a}$$

where the entries are

$$\kappa_{\rho\rho}=-\partial_{\rho\rho}\zeta, \tag{A15b}$$

$$\kappa_{\theta\theta}=-\frac{\partial_\rho\zeta}{\rho}-\frac{\partial_{\theta\theta}\zeta}{\rho^2}, \tag{A15c}$$

$$\kappa_{\rho\theta}=\kappa_{\theta\rho}=-\frac{\partial_{\rho\theta}\zeta}{\rho}+\frac{\partial_\theta\zeta}{\rho^2}. \tag{A15d}$$

3. Maxwell's equations and electric boundary conditions of thin films

We only consider the electric quantities in the thickness direction, namely

$$\boldsymbol{p}=p(z)\hat z,\quad -\nabla\xi=-\hat z\partial_z\xi=e(z)\hat z. \tag{A16}$$

It follows from (A16) that the Maxwell equation $(A7)_3$ becomes $\partial_z(\epsilon_0 e+p)=0$, $0<z<h$. Since the (free) surface charge $Q=0$ is zero here, the boundary condition $(A7)_6$ reads $\epsilon_0 e+p=0$ at $z=0,h$. The reduced Maxwell equation and boundary condition lead to the relation

$$e(z)=-p(z)/\epsilon_0. \tag{A17}$$

For thin film problems, the electric field $e(z)$ and the polarization $p(z)$ can be assumed approximately constant in the thickness direction, i.e., $e=\int_0^h e(z)dz/h$ and $p=\int_0^h p(z)dz/h$.

4. Energy formulation of thin films

The internal energy function (A9) can be recast as

$$W = W^{elast} + \frac{1}{2}ap^2 + pd_s\mathbb{I}_{2s} + pf_s\mathbb{I}_{3s} + \frac{1}{2}g\mathbb{I}_{3s}^2 \quad \text{(A18)}$$

for thin film problems. Here we choose the parameters as $\mathbb{I}_{2s} = \mathrm{tr}(\boldsymbol{E}_s)$ and $\mathbb{I}_{3s} = \mathrm{tr}(\boldsymbol{\kappa})$, that is, the trace of the in-plane strain tensor $\boldsymbol{E}_s$ in (A14) and the trace of the curvature tensor $\boldsymbol{\kappa}$ in (A15). The parameter a corresponding to the reciprocal dielectric susceptibility is $a = 1/(\epsilon - \epsilon_0)$, ϵ_0 is the vacuum permittivity and ϵ is the material permittivity. Other parameters d_s, f_s, and g are related to the piezoelectric, flexoelectric, and strain gradient effects, respectively.

It follows from $(\text{A7})_2$, (A16) and (A18) that

$$ap + d_s\mathbb{I}_{2s} + f_s\mathbb{I}_{3s} - e = 0. \quad \text{(A19)}$$

By (A17) and the parameters $\mathbb{I}_{2s} = \mathrm{tr}(\boldsymbol{E}_s)$ and $\mathbb{I}_{3s} = \mathrm{tr}(\boldsymbol{\kappa})$, we further have

$$p = -a^*\left[d_s\mathrm{tr}(\boldsymbol{E}_s) + f_s\mathrm{tr}(\boldsymbol{\kappa})\right], \quad \text{(A20)}$$

where $a^* = 1/(a + \epsilon_0^{-1})$. Typically, (A20) shows that the polarization is proportional to the mean curvature $\frac{1}{2}\mathrm{tr}(\boldsymbol{\kappa})$ in the case of non-piezoelectricity $d_s = 0$. Such a relation between the polarization and curvature is reported in a crystalline membrane [45] and in the biological context [15, 46].

For a thin dielectric disk, the thickness h is much smaller than the in-plane dimensions, we recast the elastic energy in (A3) as [44]

$$\int_{\mathcal{B}} W^{elast} dv = \frac{1}{2}\int_{\mathcal{S}} \boldsymbol{E}_s \cdot \mathbb{C}_s\boldsymbol{E}_s ds + \frac{1}{2}\int_{\mathcal{S}} C_b[\mathrm{tr}(\boldsymbol{\kappa})]^2 ds. \quad \text{(A21)}$$

The first term on the right-hand side is the stretching energy while the second term is the bending energy. Here $\boldsymbol{E}_s$ is the in-plane strain tensor (A14), $\boldsymbol{\kappa}$ is the curvature tensor (A15), $\mathbb{C}_s$ is the in-plane stiffness tensor, and C_b is the bending stiffness.

The potential work associated with the applied dead load in (A3) can be approximately as

$$-\int_{\partial\mathcal{B}_t} \boldsymbol{t}\cdot\boldsymbol{u} ds \approx -\lim_{\Delta s\to 0}(\boldsymbol{t}\cdot\boldsymbol{u})\Delta s = -Fd, \quad \text{(A22)}$$

where F is the vertical point force acting on the center of the disc film and moving at a vertical distance d.

By Eq.(A18)-Eq.(A22), the total energy Eq.(A3) specialized to the film problem becomes

$$\mathcal{F}[\boldsymbol{u}] = \frac{1}{2}\int_{\mathcal{S}} W_s ds - Fd, \quad \text{(A23)}$$

where the two-dimensional internal energy function W_s is

$$W_s = \boldsymbol{E}_s \cdot \mathbb{C}_s\boldsymbol{E}_s + (K_s + K_s^*)[\mathrm{tr}(\boldsymbol{\kappa})]^2. \quad \text{(A24)}$$

Here the coefficients K_s and K_s^* are

$$K_s = C_b + hg - ha^* f_s^2, \quad K_s^* = -ha^* f_s^2(\eta^2 + 2\eta) \quad \text{(A25)}$$

with the ratio $\eta = d_s\mathrm{tr}(\boldsymbol{E}_s)/[f_s\mathrm{tr}(\boldsymbol{\kappa})]$. Typically, in the case of non-piezoelectricity, $d_s = 0$, the ratio η and the coefficient K_s^* in Eq.(A25) are zero.

5. Units analysis

Here we would like to briefly discuss the units of symbols in the three-dimensional energy (A3) and (A9), and in the two-dimensional energy (A21), (A24), and (A25). We list the relation

$$1\ J = 1\ N\cdot m = 1\ C\cdot V.$$

In SI base units and the Named SI derived units, J represents the Joule (energy), N represents the Newton (force), m is the Metre (length), C is the Coulomb (electric charge), V is the Volt (voltage), etc. In these (three- and two-dimensional) symbols, we simply write

$$\begin{cases} \boldsymbol{p},\ p \to \dfrac{C}{m^2}, \qquad \boldsymbol{e},\ e \to \dfrac{V}{m}, \qquad \epsilon_0,\ \epsilon \to \dfrac{C}{V\cdot m}, \\ W^{elast},\ \boldsymbol{p}\cdot\boldsymbol{ap},\ \boldsymbol{p}\cdot\boldsymbol{f}\nabla\nabla\boldsymbol{u},\ \nabla\nabla\boldsymbol{u}\cdot\boldsymbol{g}\nabla\nabla\boldsymbol{u} \to \dfrac{N\cdot m}{m^3}, \\ ap^2,\ pd_s\mathrm{tr}(\boldsymbol{E}_s),\ pf_s\mathrm{tr}(\boldsymbol{\kappa}),\ g[\mathrm{tr}(\boldsymbol{\kappa})]^2 \to \dfrac{N\cdot m}{m^3}, \\ \nabla\boldsymbol{u} \to 1, \qquad \nabla\nabla\boldsymbol{u},\ \mathrm{tr}(\boldsymbol{\kappa}) \to \dfrac{1}{m}, \\ \boldsymbol{a},\ a \to \dfrac{N\cdot m^2}{C^2} = \dfrac{V\cdot m}{C}, \qquad a^* \to \dfrac{C}{V\cdot m}, \\ d_s \to \dfrac{V}{m}, \quad \boldsymbol{f},\ f_s \to \dfrac{N\cdot m}{C} = \dfrac{C\cdot V}{C} = V, \\ \boldsymbol{g},\ g \to N, \quad \mathbb{C}_s \to \dfrac{N}{m}, \quad C_b \to N\cdot m, \quad K_s \to N\cdot m. \end{cases}$$

6. Ansatz of the cone-like shape

As shown in Fig. 2 in the main paper, the initially flat sheet deforms into a cone-like shape and the surface is in partial contact with the supporting hoop. To model the developable cone, the middle surface $\mathcal{S}$ of the disc film in (A11) is divided into two parts:

$$\mathcal{S}^c = \{\boldsymbol{x} \in \mathcal{S} : 0 \leqslant \rho \leqslant R_c\}, \quad \mathcal{S}^d = \mathcal{S}\setminus\mathcal{S}^c. \quad \text{(A26)}$$

The *core* part $\mathcal{S}^c$ is the region near the tip of the developable cone and R_c can be interpreted as the core size [5, 6]. The core part of a crumpling sheet is analogous to the core of a dislocation [3, 42]. In addition, the outer region of the developable cone is represented by $\mathcal{S}^d$.

To model the conical shape of a crumpling sheet, in cylindrical coordinates, the out-of-plane deflection in (A13c) is assumed as follows:

$$\zeta(\rho,\theta)=\begin{cases}\zeta^*(\rho,\theta) & \text{on } \mathcal{S}^c,\\ \rho\psi(\theta) & \text{on } \mathcal{S}^d.\end{cases} \tag{A27}$$

Here $\psi(\theta)$ is the tangent of the slope angle of the sheet with θ the azimuthal angle, i.e. $\psi(\theta)=d/R$ if there is no crumpling and the sheet always contact the supporting hoop. The variation of the local curvature along the developable cone (d-cone) separates the d-cone into two parts [3, 4]: the concave part ($-\theta_1\leqslant\theta\leqslant\theta_1$) and the convex part ($\theta_1\leqslant\theta\leqslant 2\pi-\theta_1$). In the convex part, the surface that fully contacts the supporting hoop and forms a near-perfect circular cone except near its tip or core; while in the concave part the d-cone loses contact with the supporting hoop. Cerda and Mahadevan [3] predicted the angle (θ_1) to be: $\theta_1\approx 70^\circ$ while $\theta_1\approx 60^\circ$ was estimated by Chaieb et al. [4]. Here we adopt the model by Cerda and Mahadevan [3], then $\psi(\theta)$ in (A27) is written as

$$\psi(\theta)=\alpha_1\psi^*(\theta). \tag{A28}$$

Here α_1 is the ratio

$$\alpha_1=\frac{d}{R} \tag{A29}$$

of the tip deflection d to the radius R of the supporting hoop. And the function $\psi^*(\theta)$ is

$$\psi^*(\theta)=H^*(|\theta|-\theta_1)+\tilde{\psi}(\theta)H^*(\theta_1-|\theta|), \tag{A30}$$

where H^* is the Heaviside function, and

$$\tilde{\psi}(\theta)=\frac{\sin\theta_1\cos\alpha\theta-\alpha\sin\alpha\theta_1\cos\theta}{\sin\theta_1\cos\alpha\theta_1-\alpha\sin\alpha\theta_1\cos\theta_1}. \tag{A31}$$

Here α and θ_1 are two constants related to the shape of crumpling sheets. As reported: $\alpha\approx 3.8$, $\theta_1\approx 1.21$ rad ($\approx 70^\circ$) in [3]. Further, the ratio $\alpha_2=R_c/R$ defines another dimensionless number. The quantities (d,R_c) and their dimensionless proxies (α_1,α_2) are the two unknown quantities which are determined by the variational principle described earlier.

a. *Strain and curvature tensors*

The curvature of the core part is substantially large and there exist large strain and strain gradient, especially near the tip. Based on the observed deformed shape, for small deformation, the order of the strain tensor $\boldsymbol{E}_s$ and the order of the curvature tensor $\boldsymbol{\kappa}$ in the cone part $\mathcal{S}^c$ are approximated to [5, 6]

$$|\boldsymbol{E}_s|\sim\left(\alpha_1\frac{R_c}{R}\right)^2,\qquad |\boldsymbol{\kappa}|\sim\frac{\alpha_1}{R_c}\quad\text{on } \mathcal{S}^c. \tag{A32}$$

Here the norm of a tensor is defined as $|\boldsymbol{E}_s|=\sqrt{\boldsymbol{E}_s\cdot\boldsymbol{E}_s}$. Since only the orders of the two physical quantities ($|\boldsymbol{E}_s|$ and $|\boldsymbol{\kappa}|$) are given approximately in (A32), their exact magnitudes are still unknown. To amend these simplifications, we introduce two parameters $\lambda_{\boldsymbol{E}},\lambda_{\boldsymbol{\kappa}}\in\mathbb{R}$ that correspond to the purely mechanical behavior of a crumpling sheet. And the magnitude of the strain tensor is approximately $|\boldsymbol{E}_s|\approx\lambda_{\boldsymbol{E}}\left(\alpha_1\frac{R_c}{R}\right)^2$ while the magnitude of the curvature tensor is approximately $|\boldsymbol{\kappa}|\approx\lambda_{\boldsymbol{\kappa}}\frac{\alpha_1}{R_c}$. In the example of a crumpling steel sheet in Fig. A1, these two parameters are calculated as $\lambda_{\boldsymbol{E}}=5.5$ and $\lambda_{\boldsymbol{\kappa}}=5$, and our numerical results agree well with the experimental data at small deformation. Some other values of $\lambda_{\boldsymbol{E}}$ and $\lambda_{\boldsymbol{\kappa}}$, $1<\lambda_{\boldsymbol{E}},\lambda_{\boldsymbol{\kappa}}<10$, are also studied and the numerical results qualitatively agree with the experimental data but some quantitative discrepancy exist.

By (A15), (A27) and (A28), we can have the curvature tensor $\boldsymbol{\kappa}$ in the outer region $\mathcal{S}^d$. In addition, the condition of inextensibility requires that the stretching strains vanish in this region at moderate deflections [3, 44]. Thus, in the outer region $\mathcal{S}^d$ of the developable cone, we have

$$\boldsymbol{E}_s=\boldsymbol{0},\ \boldsymbol{\kappa}:=\begin{pmatrix}0 & 0\\ 0 & -\dfrac{\alpha_1}{\rho}\Psi^*(\theta)\end{pmatrix}\quad\text{on } \mathcal{S}^d. \tag{A33}$$

where $\Psi^*(\theta)=\partial_{\theta\theta}\psi^*(\theta)+\psi^*(\theta)$.

b. *Energy of the core and outer parts*

By (A32) and (A23)-(A25), the energy stored in the core part $\mathcal{S}^c$ is

$$\int_{\mathcal{S}^c}W_s ds=\frac{1}{2}\pi R_c^2\left\{C_s\lambda_{\boldsymbol{E}}^2\left(\alpha_1\frac{R_c}{R}\right)^4+(K_s+K_s^*)\lambda_{\boldsymbol{\kappa}}^2\frac{\alpha_1^2}{R_c^2}\right\}. \tag{A34}$$

The coefficients K_s and K_s^* are defined in (A25), and η in K_s^* here is $\eta=\bar{\eta}\alpha_1\left(\frac{R_c}{R}\right)^3$ with $\bar{\eta}=Rd_s\lambda_{\boldsymbol{E}}/(f_s\lambda_{\boldsymbol{\kappa}})$.

By (A33) and (A23)-(A25), the energy stored in the outer part $\mathcal{S}^d$ is

$$\int_{\mathcal{S}^d}W_s ds=\frac{1}{2}K_s\alpha_1^2\left(\ln\frac{R_p}{R_c}\right)\int_{-\pi}^{\pi}[\Psi^*(\theta)]^2 d\theta. \tag{A35}$$

Appendix B: Scaling of the theoretical model

The non-dimensional variables are defined by

$$\alpha_1=\frac{d}{R},\quad \alpha_2=\frac{R_c}{R}. \tag{B.1}$$

Here R is the radius of the supporting hoop, d is the unknown deflection of the disc center, and R_c is

the unknown radius of the core part. Also, other non-dimensional quantities are

$$\bar{R}_p = \frac{R_p}{R}, \quad \bar{h} = \frac{h}{R}, \quad \bar{\rho} = \frac{\rho}{R}, \quad \bar{\theta} = \frac{\theta}{\pi}, \tag{B.2}$$

$$\begin{cases} \bar{\boldsymbol{\kappa}} = \boldsymbol{\kappa} \Big/ \dfrac{1}{h},\ \bar{a} = a \Big/ \dfrac{1}{\epsilon_0},\ \bar{a}^* = a^*/\epsilon_0, \\ \bar{f}_s = f_s \Big/ \sqrt{\dfrac{1}{\epsilon_0}\dfrac{C_b}{h}},\ \bar{g} = g \Big/ \dfrac{C_b}{h}, \\ \bar{K}_s = K_s/C_b = \left(C_b + hg - ha^* f_s^2\right) \Big/ C_b, \\ \bar{C}_s = C_s \Big/ \dfrac{C_b}{h^2},\ \bar{W}_s = W_s \Big/ \dfrac{C_b}{h^2}, \\ ha^* f_s^2 \Big/ C_b = \bar{a}^* \bar{f}_s^2, \\ \bar{K}_s^* = -ha^* f_s^2(\eta^2 + 2\eta) \Big/ C_b = -\bar{a}^* \bar{f}_s^2(\bar{\eta}^2\alpha_1^2\alpha_2^6 + 2\bar{\eta}\alpha_1\alpha_2^3). \end{cases} \tag{B.3}$$

1. Dimensionless energy

By using the non-dimensional quantities (B.1)−(B.3), the dimensionless energy of the core part (A34) becomes

$$\begin{aligned} &\int_{\mathcal{S}^c} W_s ds \Big/ \left(\frac{1}{2}\pi R^2 \frac{C_b}{h^2}\right) \\ &= \bar{C}_s \lambda_{\boldsymbol{E}}^2 \alpha_1^4 \alpha_2^6 + \bar{K}_s \bar{h}^2 \lambda_{\boldsymbol{\kappa}}^2 \alpha_1^2 - \bar{a}^* \bar{f}_s^2 \bar{h}^2 \lambda_{\boldsymbol{\kappa}}^2 (\bar{\eta}^2 \alpha_1^4 \alpha_2^6 + 2\bar{\eta}\alpha_1^3\alpha_2^3) \end{aligned} \tag{B.4}$$

and the dimensionless energy of the outer region (A35) reads

$$\int_{\mathcal{S}^d} W_s ds \Big/ \left(\frac{1}{2}\pi R^2 \frac{C_b}{h^2}\right) = I_1 \bar{K}_s \bar{h}^2 \alpha_1^2 \ln(\bar{R}_p \alpha_2^{-1}), \tag{B.5}$$

where $I_1 = \int_{-1}^{1} [\Psi^*(\pi\bar{\theta})]^2 d\bar{\theta}$. The dimensionless energy associated with the external force (A22) is

$$-FR\alpha_1 \Big/ \left(\frac{1}{2}\pi R^2 \frac{C_b}{h^2}\right) = -\bar{F}\alpha_1. \tag{B.6}$$

Finally, the dimensionless total energy reads

$$\begin{aligned} \bar{\mathcal{F}}[\alpha_1, \alpha_2] &= \mathcal{F}[\alpha_1, \alpha_2] \Big/ \left(\frac{1}{2}\pi R^2 \frac{C_b}{h^2}\right) \\ &= \bar{C}_s \lambda_{\boldsymbol{E}}^2 \alpha_1^4 \alpha_2^6 + \bar{K}_s \bar{h}^2 \left[\lambda_{\boldsymbol{\kappa}}^2 + I_1 \ln(\bar{R}_p \alpha_2^{-1})\right] \alpha_1^2 \\ &\quad - \bar{F}\alpha_1 - \bar{a}^* \bar{f}_s^2 \bar{h}^2 \lambda_{\boldsymbol{\kappa}}^2 (\bar{\eta}^2 \alpha_1^4 \alpha_2^6 + 2\bar{\eta}\alpha_1^3\alpha_2^3). \end{aligned} \tag{B.7}$$

2. The governing equations

The first variation of the total energy (B.7) now reads $\delta\bar{\mathcal{F}}[\alpha_1, \alpha_2] = 0$, yields

$$\frac{\partial \bar{\mathcal{F}}[\alpha_1, \alpha_2]}{\partial \alpha_1} = 0, \quad \frac{\partial \bar{\mathcal{F}}[\alpha_1, \alpha_2]}{\partial \alpha_2} = 0. \tag{B.8}$$

Solution of the two algebraic equations in (B.8) gives the center deflection $\alpha_1 = d/R$ and the core radius $\alpha_2 = R_c/R$. Thus the curvature of each part (the core part $\mathcal{S}^c$ and the outer part $\mathcal{S}^d$) can be obtained by using (A32) and (A33). After obtaining the curvature, we can have the generated polarization p through the relation (A20). We can define the average polarization through $p^{aver} = \left(\int_{\mathcal{S}} p ds\right)/(\pi R_p^2)$. And by using the relation (A17), the average electric field is $-p^{aver}/\epsilon_0$ and the average voltage difference between the upper and lower surfaces of the crumpling thin film is determined as $|\Delta\xi| = |hp^{aver}/\epsilon_0|$.

Appendix C: Validation of the theoretical model

1. The purely mechanical crumpling

Before interrogating our model for insights into crumpling induced energy harvesting, we believe it is worthwhile to validate its prediction against established literature for the purely mechanical case. In our model, the dimensionless tip deflection $\alpha_1 = d/R$ and the radius of core part $R_c = R\alpha_2$ are calculated by solving the two algebraic equations in (B.8). The geometrical and material parameters are set to be the same as those reported in [5], thin sheets of steel with bending stiffness $7.76 \times 10^{-3} Nm$ and thickness $h = 0.075mm$. Excellent agreement between our numerical results and the experimental data in [5] is found for small deformation (circles in Fig. A1). For relatively large deformation (rhombi in Fig. S1(a) with $\alpha_1 > 0.1$), the agreement is not perfect but accounting for that is not the focus of this work. Our central goal is to achieve sufficient accuracy (and correct qualitative behavior) to account for piezoelectric and flexoelectric response of crumpling sheets, which we discuss in the main paper.

2. The generated voltage of crumpling sheets on different supporting hoops

In a recent work, Kodali et al. [37] experimented to measure the open circuit voltage and the short circuit current of a crumpling circular composite sheet. The composite sheet was made of a $52\mu m$ thick poly vinyldenefluoride (PVDF)—a known piezoelectric polymer—with electrodes on both sides and bonded to a soft cloth-plaster. The circular sheet was placed on a supporting hoop and then a concentrated vertical force was applied at the sheet center to form the crumpling shape. For different radii of the supporting hoop $R = (12.5, 20, 25)mm$, as shown in Fig. A2, roughly 0.06 V was measured by pushing the center of the circular sheet (with radius $50mm$) into a supporting hoop up to the maximum depth ($\approx 4mm$).

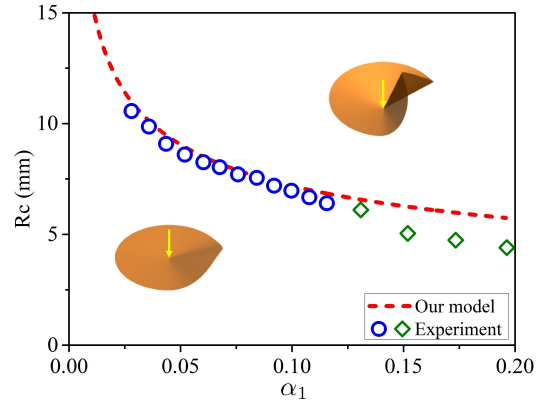

(a)

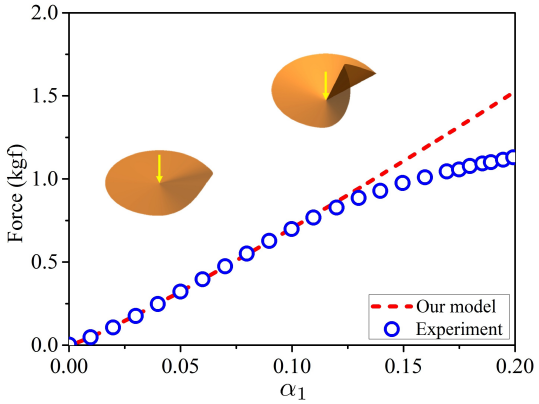

(b)

FIG. A1. Comparison of our model with the experimental data reported in [5] for the purely mechanical problem of a crumpling sheet. (a) The dimensionless tip deflection $\alpha_1 = d/R$ *vs* the radius of core part $R_c = R\alpha_2$ of a crumpling sheet. (b) The dimensionless tip deflection α_1 *vs* the vertical force F applied on the center of a thin sheet of steel. The vertical force is approximately linear with the tip deflection for small deformation. This linear relation is analogous to the relation between the center load and the maximum deflection of a simply supported beam. Note the notation difference that, in [5], the tip deflection (horizontal axis) is denoted by $\epsilon = d/R$.

In our theoretical model, the flexoelectric constant is chosen as $f_s = -179Nm/C$ [21]. By the scaling analysis in (B.3), the length scale related to the flexoelectricity can be approximately calculated as: $\sim |f_s|/\sqrt{E/\epsilon_0}$. With the parameters $|f_s| = 179Nm/C$, $\epsilon_0 = 8.85 \times 10^{-12}F/m$, and Young's modulus $E = 5GPa$ in the experiment [37], we have $|f_s|/\sqrt{E/\epsilon_0} = 7.53 \times 10^{-9}m \sim 10nm$. Thus the length scale of flexoelectricity is in nanoscale. We can also simply study the flexoelectric effect by checking the coefficient K_s in (A25) as follows: the ratio of the bending stiffness to the flexoelectric part, i.e., $C_b/(ha^*f_s^2)$. In the microscale $h \sim 10^{-6}m$, the bending stiffness $C_b \sim Eh^3 \sim 5 \times 10^{-9}Nm$, and the flexoelectric part $ha^*f_s^2 \sim 10^{-6} \times 8.85 \times 10^{-12} \times 179^2 Nm \sim 2.8 \times 10^{-13}Nm$, thus C_b is 10^4 times higher than the flexoelectric part at the microscale. In the nanoscale $h \sim 10^{-9}m$, $C_b \sim Eh^3 \sim 5 \times 10^{-18}Nm$, and $ha^*f_s^2 \sim 2.8 \times 10^{-16}Nm$, the flexoelectric part is 10^2 times higher than C_b at the nanoscale, which cannot be omitted. The nonlocal elastic constant g related to the material length l_0 as $g = El_0^2$, where E is Young's modulus of the composite sheet and l_0 is the radius of gyration of PVDF. The magnitude of l_0 in PVDF is about $10nm$ to $100nm$, and Young's modulus of PVDF is $E = 5GPa$. Thus, $g = El_0^2 \sim 10^9 \cdot 10^{-16}N = 10^{-7}N$, which is the same of order of g for PVDF used in the work [21]. In the numerical calculation, we choose $l_0 = 20nm$. The sheet thickness used in the experiment [37] is $h = 52\mu m \sim 10^{-5}m$ and the bending stiffness $C_b \sim Eh^3 \sim 10^9 \cdot 10^{-15}Nm = 10^{-6}Nm$. Since $C_b \sim 10^{-6}Nm \gg gh \sim 10^{-7} \cdot 10^{-5}Nm = 10^{-12}Nm$ in (A25), the effect of the nonlocal elastic constant g on the deformation is negligible. We also have confirmed this negligible effect by setting $g = 0$ in an extra numerical calculations. The geometrical and material parameters of a circular composite sheet in the crumpling experiment [37] are: $R_p = 50mm$, $h = 52\mu m$, $E = 5GPa$, $d_{31} = 5pC/N$, and $\epsilon = 88.5 \times 10^{-12}F/m$. Using our model, we partition the total voltage obtained into that due to flexoelectricity (FL voltage) and piezoelectricity (PZ voltage).

In Fig. A2, there are three different supporting hoops, $R = (12.5, 20, 25)mm$, and the voltage is measured when the tip deflection d increases to $4mm$ in each supporting hoop. The measured voltage can be found in Fig. 2(g) in [37]. With the ratio $\alpha_1 = d/R$, the experiments with three different supporting hoops correspond to, respectively, $\alpha_1 = 0.32, 0.20, 0.16$. In Fig. A2, at a fixed tip deflection $4mm$, both the theoretical and experimental results show that the generated voltage of crumpling sheets gradually decreases with the increase of the radius R of the supporting hoop. Furthermore, the generated voltage of the crumpling sheet decreases with the decrease of the ratio α_1. In the limiting case $\alpha_1 \to 0$, the generated voltage from the trend shown in Fig. A2 would decrease to zero. The prediction of the limiting case can be understood as follows: A sufficiently large hoop radius R corresponds to a large circular sheet ($R_p > R$), and a small deflection d cannot make the large sheet crumpled when the supporting hoop is also sufficiently large; therefore, a small deflected sheet ($\alpha_1 \to 0$) with small strain and strain gradient can only have a diminutive electromechanical coupling and generate a negligible voltage. From the above discussion, we find that the generated voltage decreases as the decrease of the ratio α_1. In other words, a higher voltage corresponds to a larger ratio α_1, and one can obtain a high voltage by increasing the tip deflection d and making a more

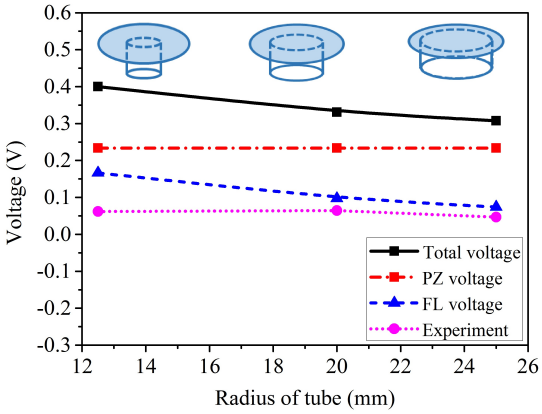

FIG. A2. Comparisons of the generated voltage of a crumpling sheet predicted by our model with the experimental data by Kodali et al. [37] with different supporting hoops. In our model, we consider both the contributions of piezoelectricity and flexoelectricity while the experiments can only calibrate the total voltage on the upper and lower surfaces of a crumpling sheet.

crumpled sheet. This prediction is also verified both theoretically and experimentally in Fig. 3 in the main paper.

It is evident that the experimental data are lower than the theoretical results in Fig. A2. One cause of the discrepancy is the presence of the load impedance in experiments and the measured voltage depends on the velocity of the actuator. However, the experimental data in Fig. A2 correspond to a actuator velocity $0.2mm/s$ and the load impedance makes the measured voltage much lower than the real generated one as well as the theoretical results. In figure 2(d) in [37], for example, the measure voltage at $d = 4mm$ is about $0.15V$ when the actuator velocity is $2mm/s$, which is much higher than the voltage $0.06V$ that is calibrated at a velocity $0.2mm/s$. Although there is some quantitative discrepancy between the theoretical and experimental results in Fig. A2 due to the existence of impedance in calibration, there is no qualitative change, and the quantitative departure from the experimental results is insignificant from an engineering viewpoint (and given the other uncertainties in material properties used in our theoretical model).

ACKNOWLEDGMENTS

B.W. was supported by the National Natural Science Foundation of China (Grant 11672164), the Natural Science Foundation of Shandong Province of China (ZR2017MA037) and the China Scholarship Council. P. S. would like to gratefully acknowledge support from the M. D. Anderson Professorship and the National Science Foundation (NSF) (Grant 1463205).

[1] A. Lobkovsky, S. Gentges, H. Li, D. Morse, and T. Witten, Science **270**, 1482 (1995).
[2] M. B. Amar and Y. Pomeau, in *Proceedings of the Royal Society of London A: Mathematical, Physical and Engineering Sciences* (The Royal Society, 1997), vol. 453, pp. 729–755.
[3] E. Cerda and L. Mahadevan, Physical Review Letters **80**, 2358 (1998).
[4] S. Chaïeb, F. Melo, and J.-C. Géminard, Physical review letters **80**, 2354 (1998).
[5] E. Cerda, S. Chaieb, F. Melo, and L. Mahadevan, Nature **401**, 46 (1999).
[6] E. Cerda and L. Mahadevan, in *Proceedings of the Royal Society of London A: Mathematical, Physical and Engineering Sciences* (The Royal Society, 2005), vol. 461, pp. 671–700.
[7] K. Matan, R. B. Williams, T. A. Witten, and S. R. Nagel, Physical Review Letters **88**, 076101 (2002).
[8] M. Marder, R. D. Deegan, and E. Sharon, Physics Today **60**, 33 (2007).
[9] A. Tagantsev, Physical Review B **34**, 5883 (1986).
[10] L. E. Cross, Journal of Materials Science **41**, 53 (2006).
[11] A. K. Tagantsev, V. Meunier, and P. Sharma, MRS bulletin **34**, 643 (2009).
[12] P. Zubko, G. Catalan, and A. K. Tagantsev, Annual Review of Materials Research **43**, 387 (2013).
[13] P. Yudin and A. Tagantsev, Nanotechnology **24**, 432001 (2013).
[14] T. D. Nguyen, S. Mao, Y.-W. Yeh, P. K. Purohit, and M. C. McAlpine, Advanced Materials **25**, 946 (2013).
[15] F. Ahmadpoor and P. Sharma, Nanoscale **7**, 16555 (2015).
[16] S. Krichen and P. Sharma, Journal of Applied Mechanics **83**, 030801 (2016).
[17] Q. Deng, L. Liu, and P. Sharma, Journal of the Mechanics and Physics of Solids **62**, 209 (2014).
[18] N. D. Sharma, R. Maranganti, and P. Sharma, Journal of the Mechanics and Physics of Solids **55**, 2328 (2007).
[19] N. D. Sharma, C. M. Landis, and P. Sharma, Journal of Applied Physics **108**, 523 (2010).
[20] S. Chandratre and P. Sharma, Applied Physics Letters **100**, 183 (2012).
[21] Q. Deng, M. Kammoun, A. Erturk, and P. Sharma, International Journal of Solids and Structures **51**, 3218 (2014).
[22] X. Jiang, W. Huang, and S. Zhang, Nano Energy **2**, 1079 (2013).
[23] M. S. Majdoub, P. Sharma, and T. Çağin, Physical Review B Condensed Matter **78**, (2008).
[24] M. S. Majdoub, P. Sharma, and T. Çağin, Phys. Rev. B **79**, 159901 (2009), URL `https://link.aps.org/doi/10.1103/PhysRevB.79.159901`.

[25] G. Catalan, A. Lubk, A. H. Vlooswijk, E. Snoeck, C. Magen, A. Janssens, G. Rispens, G. Rijnders, D. H. Blank, and B. Noheda, Nature Materials **10**, 963 (2011).
[26] M. D. Glinchuk, E. A. Eliseev, and A. N. Morozovska, Ferroelectrics **500**, 90 (2016).
[27] Y. Cao, A. Morozovska, and S. V. Kalinin, Physical Review B **96**, 184109 (2017).
[28] U. K. Bhaskar, N. Banerjee, A. Abdollahi, E. Solanas, G. Rijnders, and G. Catalan, Nanoscale **8**, 1293 (2016).
[29] U. K. Bhaskar, N. Banerjee, A. Abdollahi, Z. Wang, D. G. Schlom, G. Rijnders, and G. Catalan, Nature Nanotechnology **11**, 263 (2015).
[30] Z. Wang, X. X. Zhang, X. Wang, W. Yue, J. Li, J. Miao, and W. Zhu, Advanced Functional Materials **23**, 124 (2013).
[31] S. Mao and P. K. Purohit, Journal of the Mechanics and Physics of Solids **84**, 95 (2015).
[32] A. G. Petrov, Analytica Chimica Acta **568**, 70 (2006).
[33] W. E. Brownell, A. A. Spector, R. M. Raphael, and A. S. Popel, Annual Review of Biomedical Engineering **3**, 169 (2001).
[34] L. Liu and P. Sharma, Physical Review E **87**, 032715 (2013).
[35] J. Y. Fu, W. Zhu, N. Li, and N. B. Smith, Applied Physics Letters **91**, 2069 (2007).
[36] T. Dumitrică, C. M. Landis, and B. I. Yakobson, Chemical Physics Letters **360**, 182 (2002).
[37] P. Kodali, G. Saravanavel, and S. Sambandan, Flexible and Printed Electronics **2**, 035005 (2017).
[38] E. M. Kramer and T. A. Witten, Physical Review Letters **78**, 1303 (1996).
[39] A. E. Lobkovsky, Physical Review E **53**, 3750 (1996).
[40] S. Müller and H. Olbermann, Calculus of Variations and Partial Differential Equations **49**, 1177 (2014).
[41] J. Brandman, R. V. Kohn, and H.-M. Nguyen, Journal of Elasticity **113**, 251 (2013).
[42] F. R. Nabarro, *Theory of crystal dislocations* (Dover, New York, 1993).
[43] E. Sahin and S. Dost, International journal of engineering science **26**, 1231 (1988).
[44] L. D. Landau and E. Lifshitz, *Theory of Elasticity* (Pergamon, New York, 1986).
[45] S. V. Kalinin and V. Meunier, Physical Review B **77**, 033403 (2008).
[46] A. G. Petrov, *The lyotropic state of matter: molecular physics and living matter physics* (CRC Press, 2014).